Nonlinear Evolution of Instabilities in a Laminar Separation Bubble at Hypersonic Mach Number

Fei Li* and Meelan Choudhari†
NASA Langley Research Center, Hampton, VA, 23681

Pedro Paredes‡
National Institute of Aerospace, Hampton, VA, 23666

Anton Scholten§
North Carolina State University, Raleigh, NC, 27695

The development of both convective stationary perturbation as well as global instabilities in the vicinity of a laminar separation bubble above an axisymmetric compression corner in a hypersonic flow is investigated using numerical simulations. The flow configuration of primary interest corresponds to the cone-cylinder-flare model used in experimental measurements in the Boeing/AFOSR Mach-6 Quiet Tunnel at Purdue University. For a flare angle of 10 degrees and a unit Reynolds number of 11.5×10^6 m^{-1}, their surface flow visualizations identified the presence of streamwise elongated thermal streaks near the reattachment position and the dominant azimuthal spacing between the streaks was determined to be approximately 10 degrees (i.e., an azimuthal mode number of 36). Previous linear stability analyses predicted that the amplification characteristics of small amplitude, unsteady, convective instabilities within this flow were consistent with the surface pressure fluctuations measured in the experiment. However, their accompanying analysis of global instabilities had found the separation bubble to be weakly unstable at the 10 degrees flare angle, with the most unstable global mode corresponding to a stationary disturbance with an azimuthal wavenumber of $m \approx 5$, which was well below the measured wavenumber of $m = 36$. Besides confirming the presence of the global instability at these flow conditions, the present numerical simulations quantify the details of the stationary equilibrium state associated with the supercritical bifurcation resulting from the nonlinear saturation of the unstable global mode. Although velocity perturbations associated with the saturated global mode are dominated by the fundamental spanwise wavelength associated with the linear global instability, the surface heat flux downstream of reattachment is dominated by $m = 36$ in agreement with experimental measurements. An additional simulation of the combined evolution of both unsteady convective and global instabilities indicates that the nonlinear interactions between a broadband spectrum of oblique Mack's first mode instabilities generate stationary vortex modes with a higher dominant wavenumber ($m = 60$) as that observed in the experiments. Additional analyses are performed to predict the global mode behavior at other flare angles and how it differs from the convective centrifugal instability due to concave streamline curvature over the compression corner.

Nomenclature

f	=	disturbance frequency [kHz]
m	=	azimuthal wavenumber [nondimensional]
L	=	cone length [m]
L_s	=	separation length measured along the surface contour [m]
M	=	Mach number [nondimensional]
r	=	radial coordinate [m]
Re_∞	=	unit Reynolds number based on freestream variables [m^{-1}]
T	=	Temperature [K]
(x,y,z)	=	axial and crossplane coordinates with respect to a Cartesian system centered on the nosetip [m]
θ_f	=	flare angle [degrees]
σ	=	spatial growth rate of most unstable (or least stable) global mode [m^{-1}]
ω_r	=	real part of temporal eigenvalue [(ms)$^{-1}$]
ω_i	=	imaginary part of temporal eigenvalue, i.e., temporal growth rate [(ms)$^{-1}$]

* Aerospace Technologist, Fei.Li@nasa.gov
† Aerospace Technologist, Meelan.M.Choudhari@nasa.gov, Fellow, AIAA.
‡ Research Engineer, pedro.paredes@nasa.gov, Senior Member, AIAA.
§ Graduate Student, anton.scholten@nasa.gov, Department of Mechanical and Aerospace Engineering, AIAA Student Memebr.

Subscripts
∞ = freestream condition
i = imaginary part
r = real part
w = wall

I. Introduction

The ability to adequately predict viscous flows with boundary-layer transition and flow separation, according to the CFD Vision 2030 [1], is the most crucial issue in computational fluid dynamics (CFD) simulation capabilities that will remain a pace item for the foreseeable future. When the transition process is closely coupled with separation and the flow includes discontinuities in the form of shocks, the prediction of transition becomes much more difficult. This scenario frequently occurs in high-speed systems with compression corners when the boundary layer flow upstream of the compression corner is laminar. The laminar boundary layer cannot negotiate the unfavorable pressure gradient created by the shock near the corner when the flow turning angle is sufficiently large. As a result, flow separation occurs and, under suitable conditions, the flow may transition to turbulence prior to reattachment. Transitional shock wave boundary layer interactions often result in higher heat loads than the heat flux values measured during fully turbulent interactions, hence prediction models that account for this mode of transition are critical. Knight and Mortazavi [2] gave a summary of the studies on hypersonic, transitional shock wave boundary layer interactions including a variety of geometric shapes. The reader is referred to Refs. [3–5] for comprehensive examinations of shock wave boundary layer interactions in general and across a broader range of Mach values from transonic to hypersonic.

Compression corners represent a commonly observed feature on hypersonic vehicles. They may occur in engine inlets or as control surfaces on the exterior of the vehicle surface. As can be observed from Refs. [6–37], shock-boundary layer interactions in the area of compression corners, as well as the effect of these interactions on the laminar-turbulent transition process in boundary-layer flow, have been the focus of increasing research activity in recent years. The experimental observations of longitudinal streaks in the region of flow reattachment [7, 9, 13, 18, 19, 28, 30, 38] have been of particular interest in these studies. The streamwise elongated streaks are accompanied by significant spanwise (or azimuthal) variations in the surface heat flux and are believed to play an important role in the laminar-turbulent transition process. Maximum heat flux variations of up to 26 percent with respect to the mean (and average variations of up to 15 percent) have been reported in the literature [19]. Three distinct explanations for the emergence of these streaks have been proposed in the previous work. The first involves stationary forcing upstream of the compression corner, which causes incoming azimuthal variations to be amplified near the compression corner, either due to centrifugal destabilization in the region of concave streamline curvature above the separated flow [8, 39, 19, 20] or due to baroclinic torque. The second theory is based on stationary, global instability modes of the spanwise/azimuthally invariant laminar basic state [21, 22, 33], and the third proposal involves nonlinear interactions between oblique Mack's first mode instabilities [32].

There are varied degrees of evidence to support each of these theories in the context of specific flow configurations. The region of concave streamline curvature near the compression corner has been proven to act as a significant amplifier of the stationary streaks seeded by upstream surface nonuniformities in both computations [8, 39] and experiments [36]. Dwivedi et al. [23] investigated the highest possible amplification of incoming stationary disturbances by using a global input–output analysis. They discovered a considerable disturbance increase across a range of spanwise wavelengths, similar to the studies of roughness-induced streaks, and the wavelength of the highest amplified disturbance matched the experimental observations [19, 20] well. In addition, their close examination of the disturbance energy budget confirmed an earlier suggestion [40] that baroclinic effects involving density gradients within the laminar basic state played the dominant role in the disturbance amplification process.

Sidharth et al. [22] discovered that when the turning angle was slightly above a threshold value, the separated flow supported an unstable, symmetry breaking, 3D global mode, whereas the study by Dwivedi et al. [23] had concentrated on flows that were globally stable. Multiple unstable modes, both stationary and nonstationary, came into play when the turning angle significantly exceeded the critical value. The

experimental value of streak spacing deduced from surface flow visualizations [13] was close to the spanwise wavelength of the linearly most unstable mode according to Sidharth et al.

Lugrin et al. [32] used numerical simulations of a transitional compression corner flow to show that the broadband, stochastic forcing used in their simulation excited oblique, convective instabilities, whose nonlinear interactions led to the formation of stationary streaks and, eventually, to the onset of laminar-turbulent transition near the reattachment location. Their simulation was able to match the measured separation length from a wind tunnel experiment [9] with the right choice of force amplitude.

As discussed above, the global mode instability is likely to play a significant role in the disturbance evolution process in a significant number of compression corner flows. However, the only comparisons of global instability predictions with the experiments have been limited to the wavelength of the streaks. Furthermore, the computational analyses pertaining to the global instability [21, 22, 33] were limited to small amplitude disturbances and the measurements used for the comparisons with the computational predictions were lacking in details, particularly in regard to the unsteady disturbances in the flow. This deficiency was partly addressed by the extensive measurements of surface pressure fluctuations and off-surface density fluctuations over a cone-cylinder-flare model in the Purdue quiet tunnel [29, 30]. In particular, the measurements in Ref. [29] for an axisymmetric separation bubble over a 7-degree half-angle cone and a flare angle of 10 degrees have enabled extensive comparisons with the computational analyses of nonstationary disturbances in the flow [26, 35]. As shown in the latter two references, the axisymmetric boundary layer flow upstream of the flare can support Mack's first mode instabilities that are most amplified when the disturbances propagate at a nonzero angle with respect to the mean flow at the edge of the boundary layer as well as Mack's second mode instabilities that are dominated by axisymmetric disturbances.

The computations from [26, 35] examined the spatial evolution of these instabilities as they pass over the separation bubble in the vicinity of the corner, yielding encouraging comparisons with the measured evolution of disturbance spectra across the separated region. The analysis from [35] also investigated whether the separated flow over the cone-cylinder-flare model could support global modes of instability that are self-sustained, and hence, amplify in time, similar to the previously mentioned works involving the simpler, flat plate-wedge configurations. At the Reynolds number condition of interest ($Re_\infty = 11.5\times10^6$/m), the computations in Ref. [35] indicated the presence of an unstable global mode with the highest amplification rate corresponding to an azimuthal wavenumber of $m = 5$. However, the wavenumber of the heat flux streaks measured in the Purdue experiment [22] was significantly larger ($m \approx 36$), raising the question about the origin of those streaks.

In this paper, we perform direct numerical simulations to extend the analysis of Ref. [35] to include nonlinear disturbance dynamics in an attempt to characterize the large-time behavior of the finite amplitude global modes as well as their interaction with other instabilities in the flow. The focus of this study is on canonical cases that are intended to provide useful insights into the flow behavior and to serve as the stepping stone to the simulations involving a stochastic, broadband forcing. The details of the model configuration and the flow solvers are given in Section 2. Initial results from the ongoing numerical simulations are described in Section 3. A brief summary of the findings and concluding remarks are presented in Section 4.

II. Flow Configuration and Numerical Methodology

A. Cone-Cylinder-Flare Model

The flow configuration of interest shown in Fig. 1 is an axisymmetric configuration with a 5-degree half angle cone as the forebody, followed by a cylindrical section, and then a flare region with specified flare angle [21, 22]. The total length of the cone is $L = 0.648$ *m* (25.53 inches). The nose radius of the cone tip is equal to 0.1 mm and the 0.127 m (i.e., 5 inches) long cylindrical section has a diameter of 0.06985 m (2.75 inches). The flare angle is equal to 10 degrees, which yields a base diameter that is equal to 0.113 m (4.45 inches).

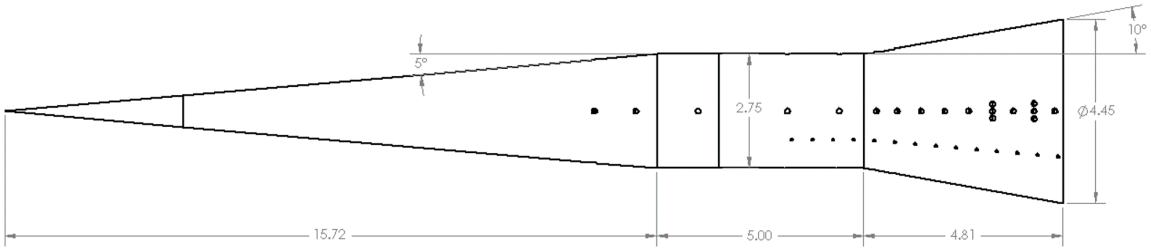

Fig. 1. Sketch of the cone-cylinder-flare model used in BAMQT experiments by Benitez et al.[11] Lengths are in inches and the angles are in degrees.

B. Flow Solvers

The unperturbed boundary layer flow along with the axisymmetric separation bubble is first computed with the VULCAN-CFD flow solver (Fig. 2), which solves the unsteady conservation equations appropriate for a laminar or turbulent flow of calorically or thermally perfect gases with a spatially second-order accurate cell-centered finite volume scheme [41]. Computations were carried out at several grid resolutions in order to obtain a shock-adapted solution for the entire cone. Then a subset of the computational domain is used for higher order accurate computations based on a 7^{th}-order spatial scheme (Fig. 2), with the inflow location at a short distance upstream of the cone-cylinder junction and extending, in the wall-normal direction, from the cone surface to just below the shock wave. The inflow and the far-field boundary conditions for this computation are obtained by using the VULCAN-CFD solution. Because the high-order code is typically used for the direct numerical simulations of transitional and turbulent flows, it will be referred to as the DNS code in this paper. A detailed description of the governing equations and the numerical algorithms used in the DNS code is given by Wu and Martin [42] and an example of the application of the DNS code can be found in Li et al. [43].

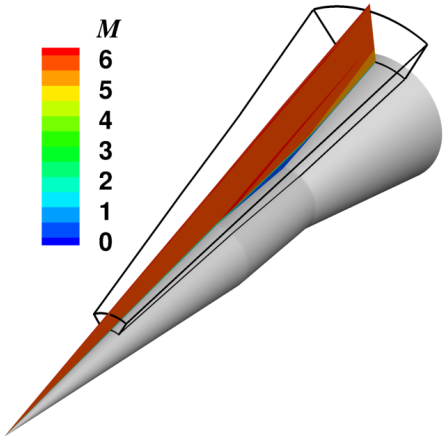

Fig. 2. DNS domain (shown as a box with black edges) along with the basic state Mach number contours along a meridional plane to illustrate the computational domain used for the VULCAN-CFD computation.

Additional computations were performed to study the development of small amplitude, linear perturbations to the axisymmetric basic state. The procedure used for the linear stability analysis involving the global modes as well as the pertinent numerical details are identical to those used in the previous work [35] and are therefore omitted for compactness. Similarly, for details on the formulation of the optimal growth calculation and the associated numerical procedures, the reader is referred to Ref. [44]. Computations of forced response to an azimuthally periodic array of small-amplitude surface deformations are also described in the section on Results. The implementation of the linearized roughness is similar to that in Ref. [45] and the solution process for the harmonic, linearized Navier-Stokes equations is the same as that used in Ref. [35].

C. Flow Conditions and Grid Details

The freestream flow conditions fall within the typical range of unit Reynolds numbers corresponding to the quiet flow operation of the Boeing/AFOSR Mach-6 Quiet-Flow Ludwieg Tube at Purdue University. Thus, the freestream Mach number M_∞ = 6, the unit Reynolds number Re_∞ = 11.5×10^6 per meter, the freestream density is ρ_∞ = 0.04526 kg/m^3, and the freestream temperature corresponds to T_∞ = 52.4 K. The temperature of the model surface, T_w, is equal to 300 K. Paredes et al. [35] investigated the linear amplification of oblique first mode waves and Mack's second mode instability for flare angles from 8 to 12 degrees and a range of nose radii. Here, we only consider the nominally sharp cone with a nose radius of 0.1 mm (i.e., with a Reynolds number based on the nose radius equal to 1150).

A variety of computational meshes were used to ensure a lack of grid sensitivity in the basic state computations with the VULCAN-CFD flow solver (Fig. 2). A rather dense mesh consisting of 3601 points in the axial direction and 1201 points along the surface normal direction was used. Special care was taken to align the streamwise grid lines with the shock front associated with the nose shock. The basic state DNS computation was limited to a computational domain that started a short distance upstream of the cone-cylinder junction. Constant temperature wall (Tw = 300 K), symmetry, and freestream boundary conditions were used for the computations.

III. Results

The numerical results presented herein are divided into multiple subsections, starting with a description of the laminar, axisymmetric basic state. As described in Section II.A, the primary flow configuration of interest in this paper corresponds to $\underline{\theta}$ = 10 degrees. However, to provide a broader context for the nonlinear analysis, we also analyze additional flare angles in the vicinity of the baseline case. Section III.A below outlines how the salient features of this basic state vary with the flare angle. Section III.B outlines the results of the linear stability analysis including both global mode analysis and optimal growth analysis of convective, stationary disturbances. The global mode analysis highlights the successive appearance of multiple unstable modes as the flare angle is increased beyond the critical flare angle that corresponds to the first onset of global instability. Section III.C presents the evolution of convective stationary perturbations over the axisymmetric laminar flow. Section III.D describes the nonlinear saturation behavior of isolated global modes corresponding to a single, dominant wavenumber from each mode family (i.e., the azimuthal wavenumber with the highest temporal growth rate). Finally, the results of a computation of unsteady, oblique first mode instabilities over the three-dimensional nonlinear equilibrium state are described in Section III.E.

A. Axisymmetric Basic State

Mach-number contours for the axisymmetric, laminar flow basic state at the flare angle of 10 degrees are shown in Fig. 3. One may observe that the initially attached flow separates from the surface at a short distance downstream of the cone-cylinder junction and reattaches again beyond the cylinder-flare junction. The region of slow-moving fluid indicated in blue includes the region of flow separation. The linear amplification characteristics of this flow were presented by Paredes et al. [35], demonstrating rather favorable comparisons with the surface pressure spectra measured by Benitez et al. [29]. Our primary concern in this paper is with the global mode evolution as discussed below.

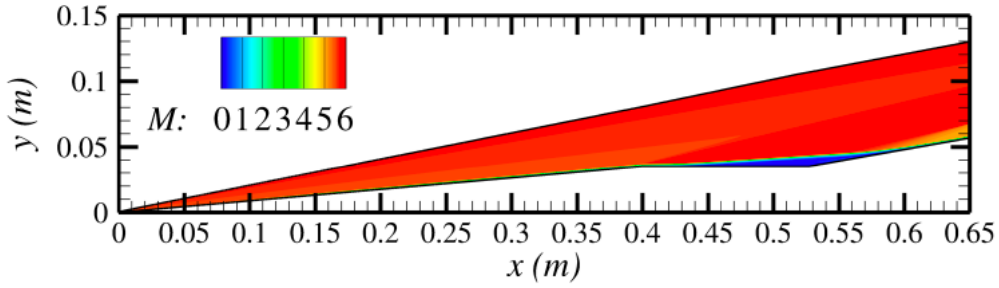

Fig. 3. Mach number contours of the laminar flow solution over the cone-cylinder-flare geometry with a flare angle of 10 degrees.

Although not shown, the flow remains fully attached for $\theta_f \leq 3.0$ degrees and the onset of separation occurs for a flare angle between $3.0 < \theta_f < 3.5$ degrees. For flare angles in the range of [4.0, 10.0] degrees, the distance between the initial separation and final reattachment points, i.e., the separation length, L_s, increases almost linearly, but the growth in separation bubble length decreases considerably for $\theta_f > 10$ degrees. Figures 4(a) and 4(b) display the axial variation in the surface pressure coefficient and skin friction coefficient, respectively, at selected values of the flare angle. Within this range of flare angles, the length of the separation bubble varies from approximately 0.14 m at a flare angle of $\theta_f = 9$ degrees to nearly 0.18 m at $\theta_f = 11$ degrees and 0.20 m at $\theta_f = 14$ degrees. These bubble lengths are comparable to the axial distance of 0.526 m from the cone tip to the compression corner, and thus, the bubble length meets the criterion for a large separation bubble [46] in that the pressure coefficient rise near the separation and reattachment regions are well separated, with a long plateau in between (Fig. 4(a)). The distribution of skin-friction coefficient in Fig. 4(b) also displays a second minimum just ahead of reattachment that is clearly the global minimum. The rise in skin friction downstream of the global minimum is steeper in comparison with the decrease to the upstream minimum near the separation point. For flare angles greater than approximately 10.3 degrees, there is secondary separation within the bubble region, similar to previous studies of planar compression corners at $\theta_f = 14$ degrees [47, 48].

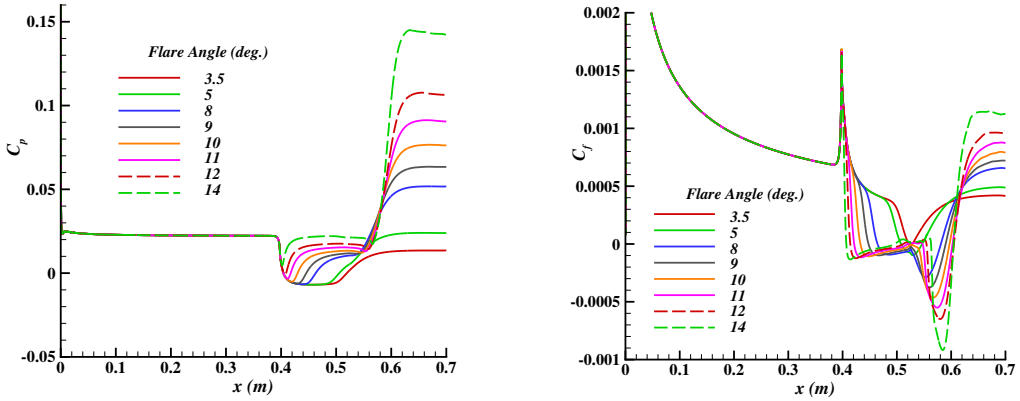

(a) Axial distribution of pressure coefficient (b) Axial distribution of skin-friction coefficient

Fig. 4. Surface flow characteristics of the axisymmetric basic state at selected values of flare angle (θ_f = 3.5, 5, 8, 9, 10, 11, 12, 14 degrees).

B. Linear Growth of Nonaxisymmetric Global Modes

Results of the linear global mode analysis by Paredes et al. [35] have shown that, at the experimental Reynolds number of $Re_\infty = 11.5\times10^6$ per meter, the separated flow near the cylinder-flare junction becomes unstable for a flare angle between 8 and 10 degrees. At 10 degrees, the flow is already moderately supercritical, with the unstable global modes spanning a finite band of azimuthal wavenumbers centered near $m = 5$. Their computations also showed that a higher flare angle of 12 degrees resulted in the onset of both nonstationary global mode instabilities and a higher wavenumber stationary mode with a peak growth rate near $m = 24$ that is more than an order of magnitude larger than the peak growth rate at the 10 degree flare angle. Given the large changes in unstable mode characteristics across the above range of flare angles, we have extended their analysis to obtain more precise estimates of the flare angle where the global modes first become unstable as well as where the nonstationary mode and the higher wavenumber stationary mode first become unstable. The overall procedure for the global mode analysis as well as the numerical details are identical to those used in the previous work [35], hence those have been omitted here for compactness.

The growth rate characteristics of the dominant families of global instabilities at a few selected flare angles are shown in Figs. 5(a)–5(d). For each flare angle, the variation in the temporal growth rate ω_i as a function of the azimuthal wavenumber m is shown on the right, whereas the corresponding values of the

radian frequency ω_r are shown on the left. For convenience, both ω_r and ω_i are expressed in terms of inverse of milliseconds. As seen from Fig. 5(a), the separated flow remains globally stable until θ_f = 9.0 degrees, where the temporal eigenvalue for a stationary mode with $m = 6$ first crosses over into the upper half of the complex ω plane. For reasons that will soon become apparent, we refer to this mode family (shown by the unstable part of the blue curve) as the long wavelength stationary mode. There are additional mode families that correspond to stable (i.e., decaying) disturbances at θ_f = 9.0 degrees and three of those families are indicated in solid red, solid green, and dashed green curves. It may be seen that the modal trajectories may come close to each other and form intricate topological connections, especially as the dispersion relationship $\omega(m;\ \theta_f)$ has square root singularities along the real m axis (even though they may not occur at integer values of m). One example of such a singularity is seen near an azimuthal wavenumber of nearly 40. Even though this singularity occurs within the stable half of the complex ω plane, the modal coalescence could well have interesting consequences in terms of temporal evolution over a finite time interval.

Three such branch points are observed in the eigenspectra at θ_f = 10.1 degrees, near $m \approx 9$, 23, and 33, respectively. Even though the long wavelength stationary mode still corresponds to the highest growth rate for $m \approx 6$, a nonstationary mode has just crossed over the real ω axis and become slightly unstable. This nonstationary mode is flanked by stationary modes on either side, namely, the long wavelength stationary modes that dominates the global mode dynamics at this flare angle and a shorter wavelength stationary mode that exists in the approximate wavenumber range of $23 < m < 33$ and corresponds to stable modes throughout that range. However, the peak growth rate associated with the short wavelength stationary mode increases at a rapid rate as the flare angle is increased from 10.1 degrees to 10.2 degrees. At θ_f = 10.2 degrees, not only has the short wavelength stationary mode become unstable, but in fact, it has the highest growth among all unstable modes. Indeed at θ_f = 10.8 degrees, the peak wavenumber as well as the peak growth rate increases from the log wavelength stationary mode to the nonstationary mode to the shorter wavelength stationary mode. The peak growth wavenumber is close to $m \approx 22$, which is closer to (yet significantly smaller than) the dominant streak wavenumber of $m \approx 36$ in the IR thermography image from Ref. [30] at the somewhat lower flare angle of θ_f = 10 degrees.

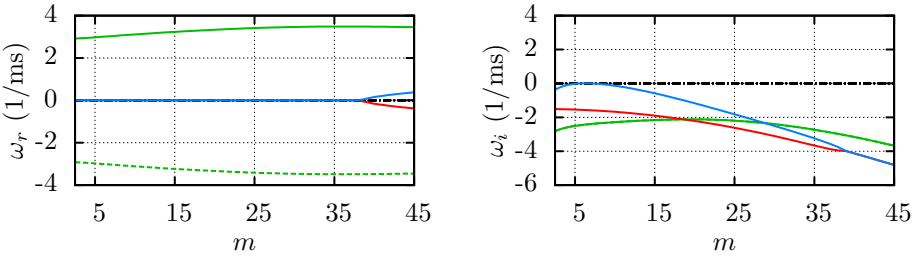

(a) θ_f = 9.0 degrees

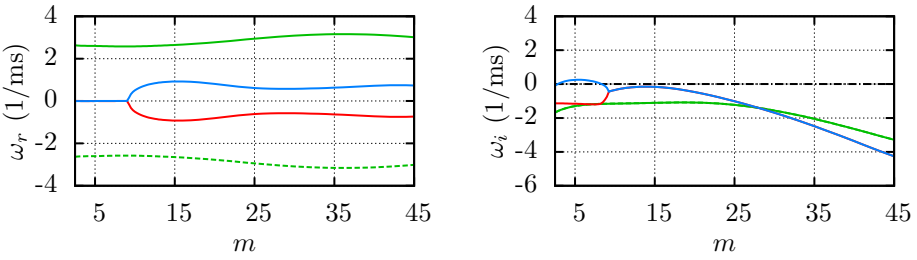

(b) θ_f = 10.0 degrees

Fig. 5. Global mode characteristics at selected values of flare angle.

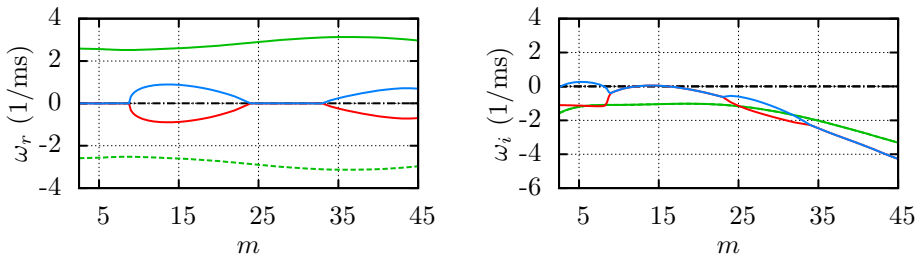

(c) θ_f = 10.1 degrees

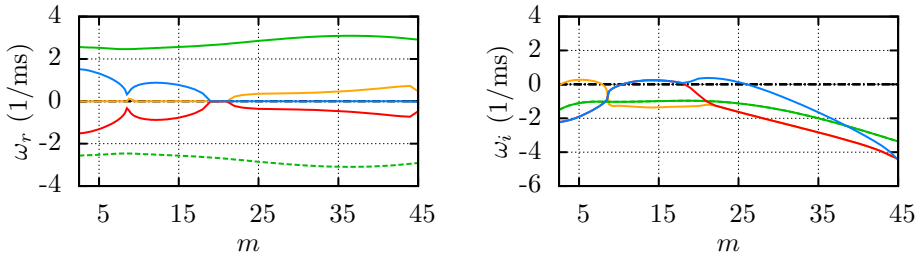

(d) θ_f = 10.2 degrees

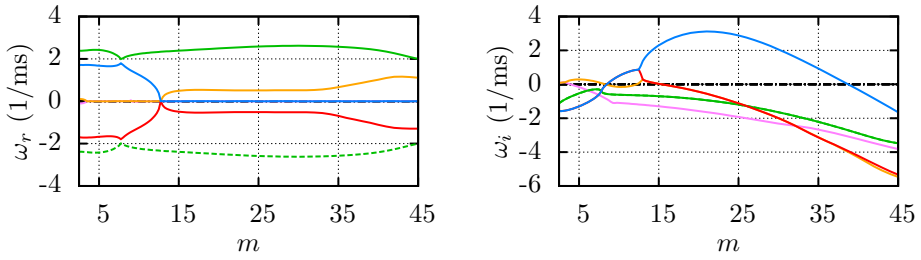

(e) θ_f = 10.8 degrees

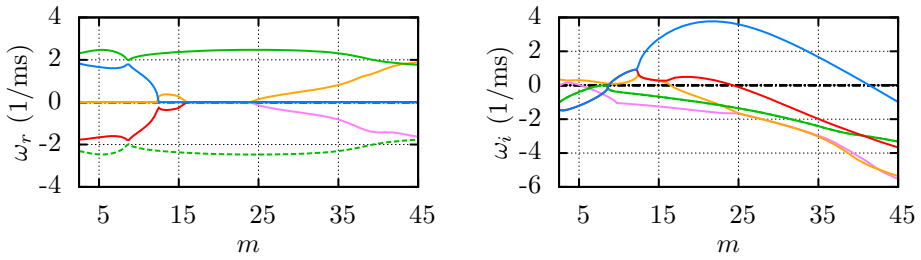

(f) θ_f = 11.0 degrees

Fig. 5. Continued.

Mode shapes for the *w*-velocity perturbation associated with selected families of global modes from Fig. 5 are shown in Figs. 6 (a) through 6 (c). Since the *w*-velocity perturbation is azimuthally antisymmetric for stationary global modes, only the nonzero imaginary part of these eigenfunctions are shown. Specifically, Fig. 6 (a) shows the mode shape for $m = 6$ at $\theta_f = 10.0$ degrees. As discussed in Ref. [35], the signature of this long wavelength stationary mode extends across the length of the separation bubble, whereas the shorter wavelength stationary mode for $m = 20$ at $\theta_f = 10.3$ degrees in Fig. 10(c) is concentrated near the reattachment location. As described previously, a nonstationary mode becomes unstable for $\theta_f >$ 10.1 degrees and Fig. 6 (b) for $m = 14$ at $\theta_f = 10.3$ degrees indicates that the signature of the nonstationary mode is also concentrated near the reattachment location. Both the real and imaginary parts of the nonstationary eigenfunction are nonzero, we show only the imaginary part here in Fig. 6 (c).

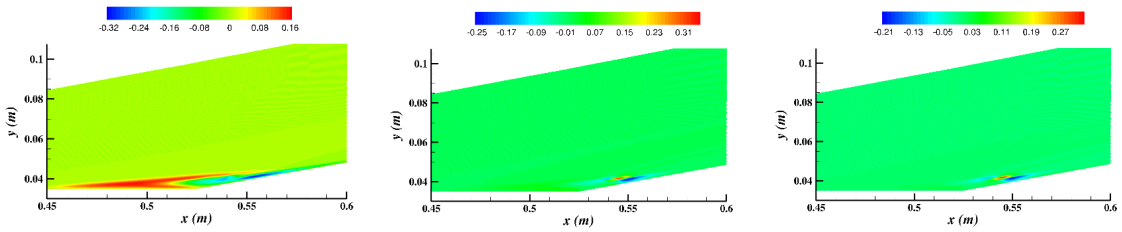

(a) $\theta_f = 10.0, m = 6$ (b) $\theta_f = 10.3, m = 14$ (c) $\theta_f = 10.3, m = 20$

Fig. 6. Mode shapes for *w*-velocity associated with selected families of unstable global modes.

The results presented in this section demonstrate that, barring certain exceptions, the global mode characteristics identified by Sidharth et al. [22] for the separation bubble over a planar compression corner are also representative of the global instability characteristics of the flare region on the axisymmetric cone-cylinder-flare model, at least within the range of flow conditions studied here, although multiple modes of instability occur for finite supercriticality (i.e., θ_f - $\theta_{f,\,onset}$ at a fixed value of Reynolds number).

C. Development of Convective Stationary Perturbations to an Axisymmetric Laminar Flow Solution

To complement the global mode analysis and to provide additional insights toward the simulations involving nonlinear disturbances in the subsequent parts of this Section, we now consider the development of stationary, azimuthally periodic disturbances to the axisymmetric laminar state for the case of θ_f = 10.0 degrees. As discussed earlier, the axisymmetric basic state is globally unstable and, therefore, is not likely to be observed in a real flow. Thus, the computation of convective perturbations in this subsection pertain to the case where disturbances at the globally unstable azimuthal wavelengths (approximately between m = 3 and m = 8) have been artificially suppressed. Two different types of analyses are performed. First, we present an optimal growth analysis that identifies the maximum possible amplification of disturbance energy over a specified axial interval [x_i, x_f]. The amplification ratio, i.e., the energy gain is defined as

$$G = E(x_f)/E(x_i)$$

where $E(x)$ represents Mack's energy norm [49] corresponding to the integrated energy at an axial station x. The wall normal integral is carried out over the entire height of the computational domain, extending from the surface to a radial location that is below the nose shock. Because the optimal growth disturbances predicted by such analysis may or may not be realized in practice, supplementary insights can be gained by studying the development of realizable disturbances due to a spatially localized forcing for one or more specific physical forms of external disturbances. The external forcing selected for the present computations corresponds to small amplitude, azimuthally periodic deformations of the surface geometry that are localized in the axial direction. Results are presented for two different array locations, one shortly downstream of the cone tip at $x \approx 0.06$ m and with an axial extent of approximately 0.004 m, and the other at $x \approx 0.38$ m and with a shorter axial extent of approximately 0.002 m.

The axial evolution of temperature perturbation amplitudes associated with the optimally growing disturbances at selected values of m is presented in Fig. 7(a). The off-body structure of the temperature perturbations for a representative wavenumber of m = 36 is shown in Fig. 7(b), wherein we emphasize the regions close to and somewhat upstream of the reattachment location. The amplitude evolution in Fig. 7(a) displays a rapid initial growth immediately downstream of the inflow station. Such rapid growth is typical of the conventional transient growth behavior in flat plate boundary layers when the inflow station is sufficiently downstream of the leading edge. The mean flow acceleration near the expansion corner at x = 0.40 m leads to a sharp decay in the streak amplitude that becomes stronger with increasing m. The disturbances at all selected wavenumbers amplify nearly monotonically over the separation bubble as well as over the region downstream of the reattachment location.

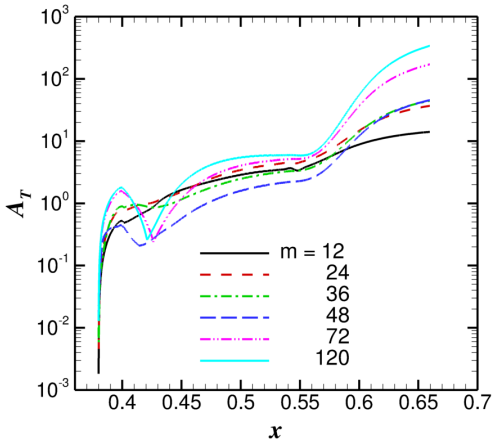

(a) Evolution of temperature perturbation amplitude for selected values of m

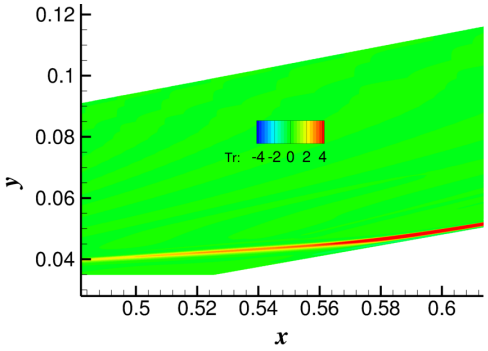

(b) Contours of temperature perturbations for $m = 36$

Fig. 7. Results of optimal growth calculations for axial interval x = [0.38, 0.65] m.

Disturbance amplification in the regions of separation and reattachment has been traditionally attributed to energy production mechanisms involving centrifugal forces associated with the concave streamline curvature in those regions. In that regard, both of the abovementioned regions of rapid disturbance amplification coincide with the highest values of concave streamline curvature. However, Dwivedi et al. [23] scrutinized the multiple physical mechanisms to show that the baroclinic terms account for a dominant part of the disturbance energy production. Overall, the growth factors for temperature perturbation amplitudes downstream of the separation location can be as high as 10^3, with the highest amplification ratios observed for the highest azimuthal wavenumbers. In other words, the optimal growth characteristics do not reveal a strong preference for the experimentally observed streak spacing with $m \approx 36$, at least for the selected axial interval of [0.38, 0.65]. The structure of the temperature perturbation contours in Fig. 7(b) indicates that the temperature perturbations induced by the optimal growth disturbance within the separation bubble are concentrated in the shear layer.

The streamwise evolution of realizable disturbances due to the two different roughness arrays is considered next. Perturbations induced by the upstream roughness array at $x \approx 0.06$ m are highly suboptimal to begin with and, although not shown, generally undergo a strong decay behind the source, before decreasing further in amplitude behind the expansion corner. The roughness array at $x \approx 0.38$ m is just upstream of the expansion corner and the resulting perturbations also exhibit a decrease in amplitude as the mean flow navigates the pressure gradient due to that corner. But, in both cases, the disturbances amplify across the separation bubble and also past the reattachment location. To highlight that growth of realizable perturbations, we plot the normalized amplitude evolution for selected azimuthal wavenumbers in Fig. 8. The temperature perturbation amplitudes at each azimuthal wavenumber are scaled by the minimum amplitude near the separation location. The qualitative evolution behind both roughness arrays is similar, except in the low wavenumber cases (m = 12 and m = 24) that also correspond to the lowest growth within the separation region. The higher wavenumber perturbations have similar amplification ratios between Figs. 8(a) and 8(b), with somewhat higher peak values for the upstream roughness array at $x \approx 0.06$ m. It is also interesting that the growth factors beyond the separation zone are also similar between the realizable disturbances in Fig. 8 and the optimal growth perturbations in Fig. 7(a).

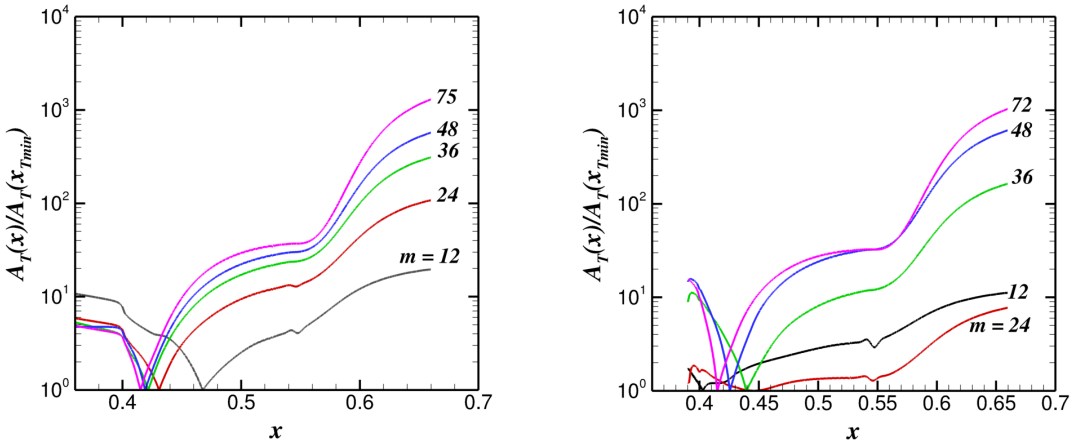

(a) $x_r \approx 0.06$ m (b) $x_r \approx 0.38$ m

Fig. 8. Streamwise evolution of gain in peak temperature perturbation. To highlight the amplification across the separation bubble, the gain curves are normalized to unity at the minimum in the vicinity of separation point.

Contours of temperature perturbation in the $z = 0$ plane are shown for a representative azimuthal wavenumber ($m = 36$) in Fig. 9. Figure 9(a) corresponds to a roughness array far upstream of the separation bubble ($x_r \approx 0.06$ m), whereas Fig. 9(b) corresponds to a roughness array just upstream of the cone cylinder junction (($x_r \approx 0.38$ m). Regardless of where the azimuthal variations were forced into the boundary layer, the peak perturbation levels at any given station inside the separation bubble are concentrated within the shear layer along the outer boundary of the bubble, except in the region of reattachment where the inner parts of the recirculating flow also exhibit significant yet smaller perturbations. The sign change in temperature perturbations also indicates an azimuthal shift in the streaks depending on the forcing location.

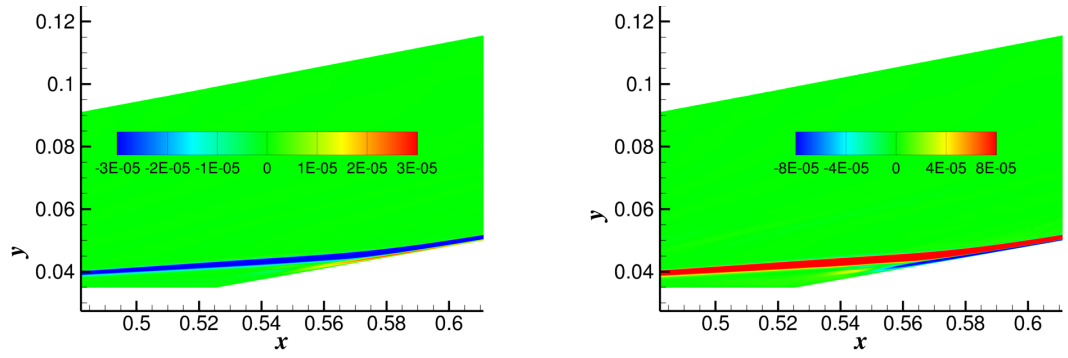

(a) $x_r \approx 0.06$ m (b) $x_r \approx 0.38$ m

Fig. 9. Contours of temperature perturbations due to a roughness array ($m = 36$).

D. Nonlinear Growth of Dominant Global Modes

DNS was used to compute the temporal evolution of nonaxisymmetric perturbations to axisymmetric basic state corresponding to the experimental configuration of $\theta_f = 10$ degrees shown in Fig. 3. We focus on the nonlinear evolution of an long wavelength stationary mode with $m = 6$ (close to the most unstable wavenumber $m = 5$). The initial perturbation was defined by assigning a small amplitude to the eigenfunction of the linear global mode. The azimuthal domain selected for the computation was such that the initial z-component of perturbation velocity is antisymmetric with respect to $z = 0$ and this antisymmetric behavior persisted throughout the temporal evolution. Analogously, the other field quantities remained symmetric with respect to the z coordinate.

Figure 10(a) shows the time history of the u-perturbation velocity as measured by five different probes in the interior of the boundary layer at $x = 0.534$ m for the abovementioned case that was seeded with an $m = 6$ global mode eigenfunction. The center probe at an azimuthal angle of $\theta = 0$ registers a maximum positive signal because of the symmetric nature of the u-perturbation. Since the wavenumber of $m = 6$ corresponds to an azimuthal wavelength of 60 degrees, four other probes are placed on one side of the symmetry plane at azimuthal intervals of 7.5 degrees each. These probes display an exponential growth of the u-perturbation following a short period of initial transient that is barely seen on the linear scale in Fig. 10(a). As the perturbation gains in amplitude, the growth rate decreases and, eventually, reduces to zero as the disturbance level asymptotes to a constant amplitude steady state. Figure 10(b) shows the normalized probe data at the 0-degree azimuthal angle on a logarithmic scale, together with the straight line prediction from linear eigenvalue analysis. The agreement between the linear (blue line) and nonlinear predictions (red curve) over a significant time interval confirms the exponential growth at earlier times and that the growth rate in the DNS matches the amplification rate predicted by the linear global mode analysis.

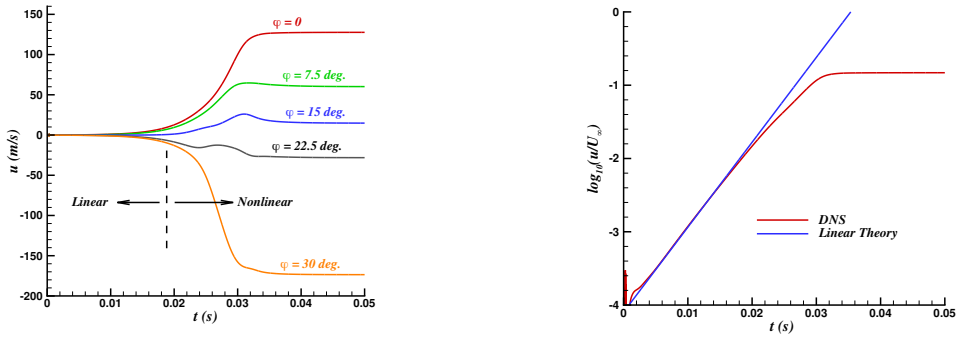

(a) Time series for five different probes on a linear scale

(b) Probe data at the 0-degree azimuthal angle on a logarithmic scale.

Fig. 10. Temporal evolution of *w*-velocity at selected probe locations.

The azimuthal Fourier decomposition associated with the nonlinear saturation state for the $m = 6$ fundamental mode is shown in Fig. 11(a). In the upstream part of the separation bubble (i.e., for x between 0.4 m and 0.5 m over the cylinder), the dominant mode in u-velocity perturbation corresponds to the mean flow correction ($m = 0$). For a short interval in the vicinity of the cylinder-flare junction, the dominant mode switches over to the fundamental mode $m = 6$, but the mean flow correction gain overtakes the fundamental amplitude. In the downstream region of $x > 0.6$ m, the first harmonic ($m = 12$) has the largest amplitude and it remains dominant until the end of the computational domain. The spanwise Fourier decomposition of the wall heat flux is shown in Fig. 11 (b). The mean flow correction amplitude is the largest over the upstream 40% of the cylinder length and in the upstream portion of the flare. In between these two regions, the fundamental mode is dominant. However, starting at approximately $x = 0.58$ m on the flare, i.e., in the vicinity of the reattachment location, the 5th harmonic ($m = 36$) becomes the dominant one, while the 2nd and 6th harmonics ($m = 12$ and 42, respectively) are also very strong.

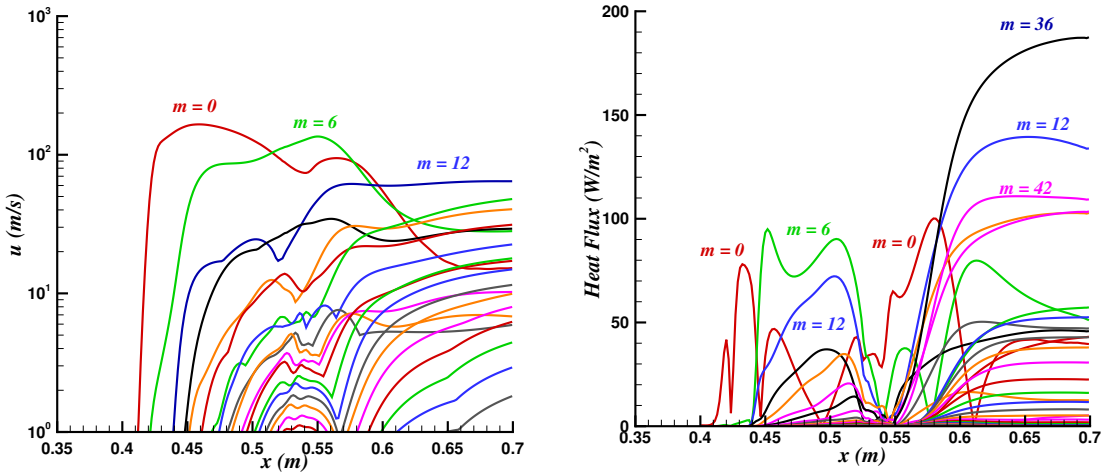

(a) u-amplitudes (b) Wall heat flux amplitudes

Fig. 11. Azimuthal Fourier decomposition of perturbation amplitudes.

Figure 12 depicts the Stanton number (nondimensional heat flux) distribution over the surface that indicates multiple thermal streaks across each azimuthal wavelength of the $m = 6$ fundamental mode. This is consistent with the amplitude evolution of the Fourier components shown in Fig. 11(b) above, which shows that short azimuthal waves dominate. The resulting azimuthal structure is analogous to that measured in the experiment. In principle, the streaks observed in the experiment are fixed by the specific combination of initial and boundary conditions associated with each realization of the flow and additional measurements are necessary to clarify whether the azimuthal locations of the naturally occurring streaks are fixed to the surface geometry, which would indicate a dominant role of the stationary forcing associated with surface roughness. The role of external conditions, combined with the small but finite bandwidth of m = [3, 8] of the global mode instability at θ_f = 10 degrees, could account for the apparently stochastic nature of the measured streaks [30], contrary to the periodic nature of the heat flux variations associated with the saturation state driven by the $m = 6$ global mode alone.

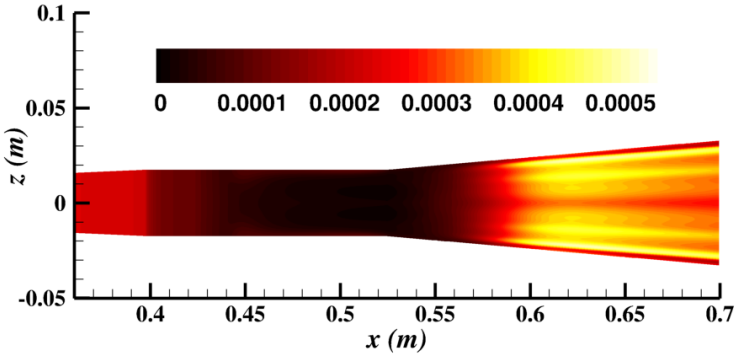

Fig. 12. Stanton number contours over the surface of the cone-cylinder-flare configuration.

The presence of the stationary global instability changes the skin-friction patterns on the surface of the cone-cylinder-flare configuration. In Figure 13, each surface line is traced out by integrating the surface skin-friction vector starting from a seed location. These lines are "trapped" within the separation bubble and end at locations where the skin friction becomes zero. The skin friction fields that lead to Figs. 13(a) through 13(c) are constructed by superimposing the linear eigenfunctions of the stationary global mode with a given amplitude on top of the base flow variables. For zero amplitude (not shown), the lines would run along the meridians of the axisymmetric cone-cylinder-flare configuration. With a scaled amplitude of 1% assigned to the global mode eigenfunction at $m = 6$, the skin friction lines converge toward the line of symmetry of the azimuthal domain shown in Fig. 13 when the axial location is upstream of the cylinder-flare junction and the

friction lines diverge downstream of that junction. As the amplitude of the linear global mode increases, a subset of the friction lines from upstream appear to converge to a single node before diverging into the region downstream of the cylinder-flare junction. However, the friction lines computed from the nonlinearly saturated solution (Fig. 11(d)) exhibit a more intricate pattern than those associated with the linear mode shape. The separation boundary appears to be similar in all cases, indicating rather small and nearly sinusoidal perturbations to the axisymmetric laminar flow. However, the reattachment boundary for the nonlinear saturation state shows distinct short-scale corrugations associated with the smaller wavelength streaks due to nonlinear effects.

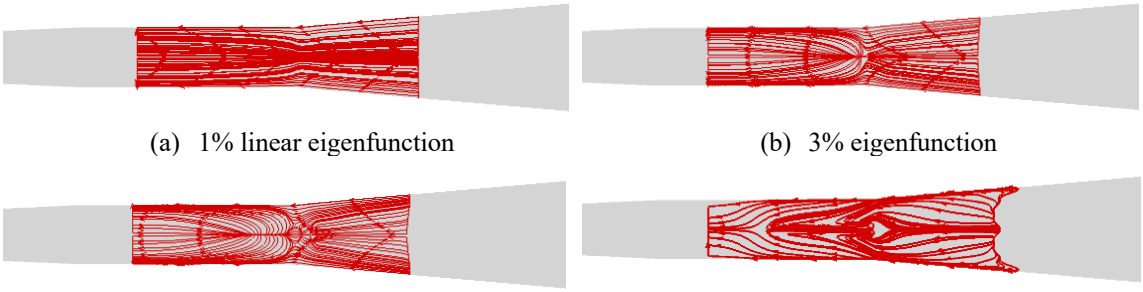

(a) 1% linear eigenfunction (b) 3% eigenfunction

(c) 5% linear eigenfunction (d) Nonlinearly saturation solution

Fig. 13. Comparison between wall-friction lines from linear, global mode eigenfunctions of different amplitudes superimposed on the axisymmetric laminar base flow and those obtained from the nonlinear saturation state.

E. Development of Perturbations to Nonlinear Equilibrium State Associated with Dominant Global Modes

In an additional simulation involving unsteady perturbations to the nonlinear saturation state resulting from the $m = 6$ global mode, a localized unsteady forcing at the wall was used to excite the boundary layer instability modes over a broad range of frequencies. The forcing strategy is analogous to that used to excite the secondary instability modes of a stationary crossflow pattern over a yawed cone in Ref. [47]. The azimuthal and time dependence of the wall-forcing function includes a superposition of time harmonic signals comprised of multiple discrete frequencies from 30 kHz to 250 kHz at an interval of 10 kHz. In particular, the forcing distribution with random phase angles, ϕ_{ij}, corresponds to a nonzero surface-normal velocity of

$$\frac{v'(x,t)}{U_\infty} = g(x)\sum_{i=1}^{n_\beta}\sum_{j=3}^{n_f} A_j \cos\left(-2\pi f_j\, t + \phi_{ij}\right) \cos(i\beta\varphi) \quad , \tag{10}$$

at the cone surface, where $g(x)$ denotes the axial distribution of the forcing amplitude. For a forcing function that begins at $x = x_b$ and ends at $x = x_e$, the shape function $g(x)$ is specified as a function of the normalized coordinate ξ that is defined as

$$\xi(x) = \big(2x - (x_e + x_b)\big)/(x_e - x_b)\ .$$

If $x \geq x_b$ and $x < x_0 \triangleq \frac{(x_e+x_b)}{2}$ (or equivalently, $0 < \xi < -1$), then

$$g(x) = \quad 1.5^4(3(1+\xi)^5 - 7(1+\xi)^4 + 4(1+\xi)^3),$$

whereas for $x \geq \frac{(x_e+x_b)}{2}$ and $x < x_e$ (or equivalently, $0 \leq \xi \leq 1$),

$$g(x) = -1.5^4(3(1-\xi)^5 - 7(1-\xi)^4 + 4(1-\xi)^3)$$

and otherwise

$$g(x) = 0.0$$

for all other x. The forcing frequencies are given by $f_j = 10 \times j$ kHz, $n_\beta = 6$ and $n_f = 25$. The range of forcing frequencies is guided by the results of the convective instability analysis in Ref. [35]. To reduce the computational cost, the unsteady forcing location of x_0 = 0.26 m is chosen to be somewhat downstream of the likely onset of first mode instability, and the width of the forcing function $g(x)$ is equal to 0.0014 m. Given the broad range of excitation frequencies, the above slot width was chosen to be sufficiently narrow so as to excite an unsteady disturbance field with a broad band of streamwise wavenumbers that are likely to couple into the unstable modes at the relevant frequencies. To investigate both a linear amplification of the flow instabilities as well as a modest nonlinear interaction that is likely to generate the streamwise vortex modes via nonlinear interactions, a suitable amplitude of the wall forcing is used, with $A_j = 2 \times 10^{-4}$ for all j. Fourier decomposition of the time history from the output signal is used to analyze the disturbance evolution at each selected frequency.

The time history of the computed solution for the forced unsteady perturbation Fourier transformed in time to isolate the different frequency components. The crossplane contours of the u-velocity perturbation at selected dominant frequencies at x = 0.64 m over the flare region are shown in Figure 14. At a frequency of 30 kHz, the perturbation amplitudes appear to concentrate near the azimuthal ends of the periodic domain extending across 60 degrees, i.e., a single wavelength of the linear global eigenmode at m = 6. For higher frequencies, comparable disturbance amplitudes are also observed near the line of symmetry at z = 0, indicating the emergence of structures with smaller azimuthal wavelengths. A crossplane plot of the perturbation u-velocity of the nonlinearly saturated stationary mode at the same streamwise location is shown in Fig. 14(f) as a comparison.

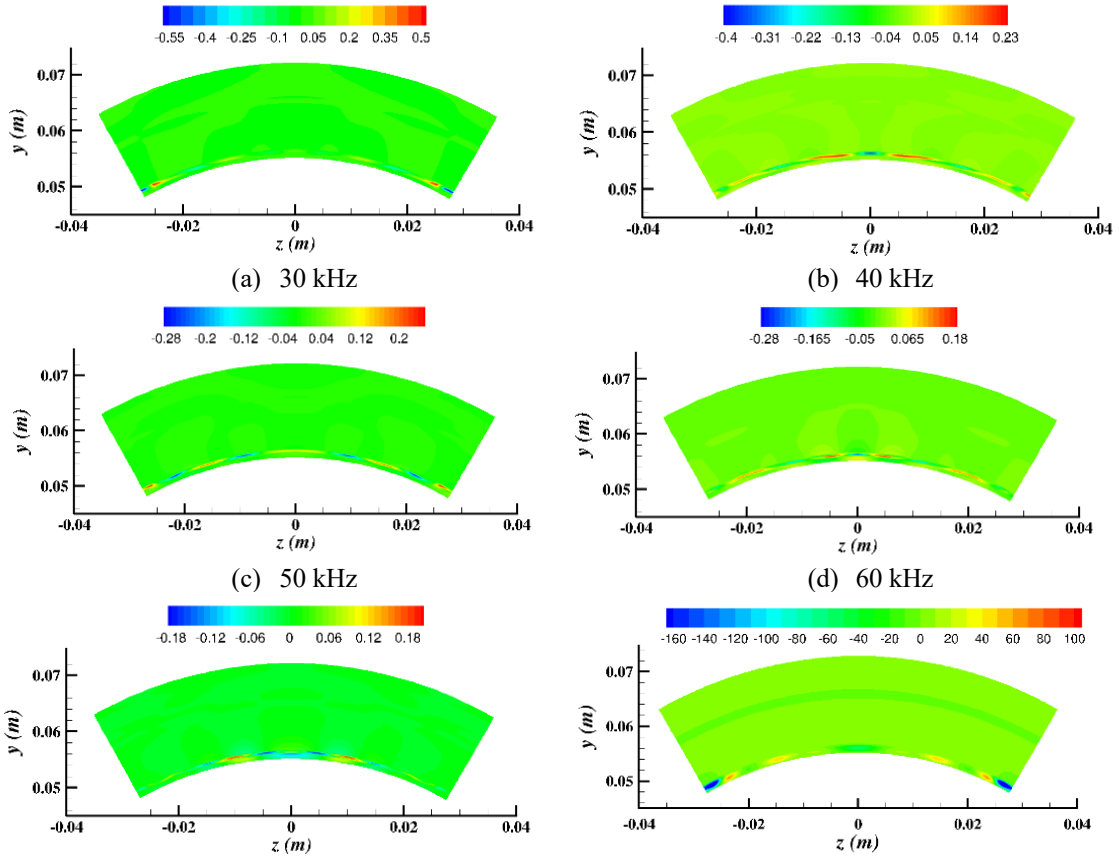

(a) 30 kHz (b) 40 kHz

(c) 50 kHz (d) 60 kHz

(e) 70 kHz (f) Saturated stationary global instability

Fig. 14. Comparison of cross-plane unsteady structures with stationary structures at x = 0.64 m

The oblique traveling modes discussed above interact nonlinearly with each other to create stationary vortex modes. To investigate the signature of the mean flow correction including those vortex modes, Fig. 15 shows the contours of the radial derivative of the temperature field associated with the mean flow correction. The radial derivative term is proportional to the time-averaged wall heat flux. The reason to isolate the perturbation contours (instead of the total heat flux contours shown in Fig. 12) is related to the rather small magnitude of the mean flow correction, presumably due to the relatively weak nonlinear effects at the forcing amplitudes used in the simulation. Strong streaky structures with an approximate azimuthal wave number of 60 are clearly seen.

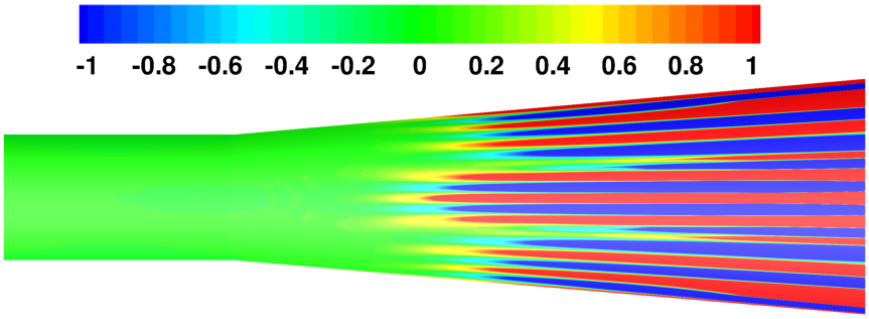

Fig. 15. dT/dr contours showing streaky structures at wall for stationary perturbations across an azimuthal domain width of 60 degrees.

IV. Summary and Concluding Remarks

The cone-cylinder-flare configuration investigated by Benitez et al. [29] exhibits a globally unstable laminar basic state, comparable to the simpler compression ramp topologies investigated in other recent investigations [22, 31, 33, 37]. However, the cone-cylinder-flare configuration differs from other works, not only due to the extensive unsteady measurements in addition to surface heat flux data in Ref. [29], but also by virtue of the completely laminar shock boundary layer interaction in this case, as opposed to the transitional interaction, for instance, in Ref. [37]. The competing hypotheses proposed in the recent studies about the nature of dominant flow instabilities and the physical mechanisms underpinning the production of longitudinal, stationary thermal streaks suggest that the dominant disturbance growth mechanisms may well be dependent on the flow geometry and the external disturbance environment.

In the current flow configuration, the separation bubble remains laminar, ensuring that the unstable disturbances are kept low. Thus, the current work aimed to improve our understanding of the instability processes of the separated flow and the significance of the multiple distinct disturbances in explaining the experimental findings of Benitez et al. [29] under low-disturbance (i.e., "quiet") freestream conditions. The findings thus far have proven the presence of the global instability and given insight into the physically rich disturbance dynamics in this flow. Three distinct hypotheses for the experimentally observed streak spacing of m = 36 were investigated in this paper, namely, (i) finite-amplitude, stationary global instabilities, (ii) convective amplification of external stationary disturbances, and (iii) stationary longitudinal vortices generated via nonlinear interactions between nonstationary, oblique first mode instabilities. The numerical investigation of the joint evolution of convective and controlled global instabilities in that flow at postcritical conditions is a novel but preliminary component of the current article.

Unlike previous analyses of global instability over simpler (and planar) compression corner flows, where the spanwise wavelength of the linearly most unstable global mode was found to correlate with the dominant spanwise spacing of stationary streaks in the experiment, the dominant global mode for the cone-cylinder-flare model of Benitez et al. [29] has a substantially lower wavenumber (m = 6) than the dominant wavenumber (m = 36) from their measurements at Re_∞ = 11.5×10^6 per meter and θ_f = 10 degrees. The azimuthal Fourier decomposition of the nonlinear saturation state resulting from the m=6 global mode shows the m=36 mode to be dominant downstream of the reattachment location. However, the nonlinear state exhibits significant variations in the strength of the streaks, in contrast with the homogenous pattern of azimuthal variations in the measured heat flux distribution [30].

An alternate theory for the formation of short wavelength streaks involved the convective, i.e., spatial amplification of externally imposed stationary perturbations. Both optimal growth theory and the forced disturbances excited by an axially localized and azimuthally periodic array of roughness elements showed strong amplification near the separation and reattachment locations. However, the convective amplification is very broadband in character, extending up to $m = 150$ and larger. While that does not preclude the existence of a spectral peak near $m = 36$ in the measured heat flux distribution, the only way that can occur is if the azimuthal wavenumber spectrum of the upstream roughness distribution on the experimental cone happens to be dominated by wavenumbers near $m = 36$. That is possible, but perhaps, rather unlikely. The third option for the observed streaks near $m = 36$ involved nonlinear mode interactions between oblique instabilities with an azimuthal wavenumber near $m = 18$. The simulation of broadband, convective disturbances seeded by a suction/blowing type wall forcing with equal amplitudes for several frequency-wavenumber pairs yields a vortex mode as part of the mean flow correction, which yields short wavelength structures with wavenumbers approaching $m = 60$.

In conclusion, the present computations predict streak spacings that are comparable to those in the experiment.. Experiments on a larger range of flow parameters (unit Reynolds number and flare angle) may yield additional hints that would help to clarify the physical mechanism(s) underlying the experimentally observed streaks, especially in laminar shock boundary layer interactions.

Acknowledgments

This work is supported by NASA's Hypersonic Technology Project. Computational resources for this research were provided by the NASA High-End Computing (HEC) Program through the NASA Advanced Supercomputing (NAS) Division at the Ames Research Center. Authors Pedro Paredes and Anton Scholten were also supported by the U.S. Office of Naval Research under award number N00014-20-1-2261.

References

[1] Slotnick, J., Khodahoust, A., Alonso, J., Darmofal, D., Gropp, W., and Mavriplis, D., "CFD Vision 2030 Study: A Path to Revolutionary Computational Aerosciences," NASA/CR-2014-218178, 2014. https://ntrs.nasa.gov/api/citations/20140003093/downloads/20140003093.pdf

[2] Knight, D. and Mortazavi, M., "Hypersonic Shock Wave Transitional Boundary Layer Interactions - A Review," *Acta Astronautica*, Vol. 151, Oct. 2018, pp. 296–317. https://doi.org/10.1016/j.actaastro.2018.06.019

[3] Delery, J., "Shock Wave/Turbulent Boundary Layer Interaction and Its Control, *Prog. Aerosp. Sci.*, Vol. 22, 1985, pp. 209–80. https://doi.org/10.1016/0376-0421(85)90001-6

[4] Babinsky H. and Harvey, J., eds., "Shock Wave-Boundary Layer Interactions," Cambridge University Press, New York, USA, 2011.

[5] Gaitonde, D. V., "Progress in Shock Wave/Boundary Layer Interactions," *Prog. Aerosp. Sci.*," Vol. 72, January 2015, pp. 80–99. https://doi.org/10.1016/j.paerosci.2014.09.002

[6] Simeonides, G. and Haase, W., "Experimental and Computational Investigations of Hypersonic Flow About Compression Ramps," *J. Fluid Mech.*, Vol. 283, pp. 17–42, 1995. https://doi.org/10.1017/S0022112095002229

[7] Matsumara, S., Schneider, S.P. and Berry, S.A., "Streamwise Vortex Instability and Transition on the Hyper-2000 Scramjet Forebody," *J. Spacecraft and Rockets*, Vol. 42 (1), pp. 78-89, 2005. https://doi.org/10.2514/1.3959

[8] Navarro-Martinez, S. and Tutty, O. R., "Numerical Simulation of Görtler Vortices in Hypersonic Compression Ramps," *Comp. Fluids*, Vol. 34 (2), pp. 225–247, 2005. https://doi.org/10.1016/j.compfluid.2004.05.002

[9] Benay, R., Chanetz, B., Mangin, B., Vandomme, L., and Perraud, J., "Shock Wave/Transitional Boundary-Layer Interactions in Hypersonic Flow," *AIAA Journal*, Vol. 44, 2006, pp. 1243–1254. https://doi.org/10.2514/1.10512

[10] Robinet, J., "Bifurcations in Shock-Wave/Laminar-Boundary-Layer Interaction: Global Instability Approach," *J. Fluid Mech.,* Vol. 579, pp. 85–112, 2007. https://doi.org/10.1017/S0022112007005095

[11] Bur, R., and Chanetz, B., "Experimental Study on the PRE-X Vehicle Focusing on the Transitional Shock-Wave/BoundaryLayer Interactions," *Aerospace Science and Technology*, Vol. 13, No. 7, 2009, pp. 393-401. https://doi.org/10.1016/j.ast.2009.09.002

[12] Brown, L. M., Boyce, R. R., Mudford, N., and Byrne, S. O., "Intrinsic Three-Dimensionality of Laminar Hypersonic Shock Wave/Boundary Layer Interactions," AIAA Paper 2009-7205, 2009. https://doi.org/10.2514/6.2009-7205

[13] Yang, L., Zare-Behtash, H., Erdem, E., and Kontis, K., "Investigation of the Double Ramp in Hypersonic Flow Using Luminescent Measurement Systems," *Exp. Thermal Fluid Sci.*, Vol. 40, 2012, pp. 50–56. https://doi.org/10.1016/j.expthermflusci.2012.01.032
[14] Murray, N., Hillier, R., and Williams, S., "Experimental investigation of axisymmetric hypersonic shock-wave/turbulent-boundary-layer interactions," *J. Fluid Mech.*, Vol. 714, pp. 152–189, 2013. https://doi.org/10.1017/jfm.2012.464
[15] Sandham, N. D., Schulein, E., Wagner, A., Willems, S., and Steelant, J., "Transitional Shock-Wave/Boundary-Layer Interactions in Hypersonic Flow," *J. Fluid Mech.,* Vol. 752, pp. 349–382, 2014. https://doi.org/10.1017/jfm.2014.333
[16] Schulein, E., "Effects of Laminar-Turbulent Transition on the Shock-Wave/Boundary-Layer Interaction," AIAA Paper 2014-3332, 2014. https://doi.org/10.2514/6.2014-3332
[17] Giepman, R.H.M, Schrijer, F.F.J., and van Oudheusden, B.W., "High-Resolution PIV Measurements of a Transitional Shock Wave-Boundary Layer Interaction," AIAA Paper 2014-3333, 2014. https://doi.org/10.2514/6.2014-3333
[18] Roghelia, A., Chuvakhov, P., Olivier, H., and Egorov, I. "Experimental Investigation of Görtler Vortices in Hypersonic Ramp Flows," AIAA Paper 2017-3463, 2017. https://doi.org/10.2514/6.2017-3463
[19] Roghelia, A., Olivier, H., Egorov, I. and Chuvakhov, P., "Experimental Investigation of Görtler Vortices in Hypersonic Ramp Flows," *Exp. Fluids*, Vol. 58 (10), p. 139, 2017. https://doi.org/10.1007/s00348-017-2422-y
[20] Chuvakhov, P. V., Borovoy, V. Y., Egorov, I. V., Radchenko , V.N., Olivier, H., and Roghelia, A., "Effect of Small Bluntness on Formation of Görtler Vortices in a Supersonic Compression Corner Flow," *J. Appl. Mech. Tech. Phys.*, Vol. 58 (6), pp. 975–989, 2017. https://doi.org/10.1134/S0021894417060037
[21] Hildebrand, N., Dwivedi, A., Nichols, J., Jovanovic, M., and Candler, G., "Simulation and Stability Analysis of Oblique Shock-Wave-Boundary-Layer Interactions at Mach 5.92," *Phys. Rev. Fluids*, Vol. 3, No. 013906, 2018. https://doi.org/10.1103/PhysRevFluids.3.013906
[22] Sidharth, G. S., Dwivedi, A., Candler, G., and Nichols, J., "Onset of Three-Dimensionality in Supersonic Flow Over a Slender Double Wedge," *Phys. Rev. Fluids*, Vol. 3, No. 093901, 2018. https://doi.org/10.1103/PhysRevFluids.3.093901
[23] Dwivedi, A., Sidharth, G. S., Nichols, J., Candler, G., and Jovanovic, M., "Reattachment Streaks in Hypersonic Compression Ramp Flow: an Input-Output Analysis," *J. Fluid Mech.*, Vol. 880, pp. 113–135, 2019. https://doi.org/10.1017/jfm.2019.702
[24] Running, C. L., Juliano, T. J., Jewell, J., Borg, M., and Kimmel, R., "Hypersonic Shock-Wave/boundary-Layer Interactions on a Cone/Flare," *Exp. Thermal and Fluid Science*, Vol. 109, 2019, 109911. https://doi.org/10.1016/j.expthermflusci.2019.109911
[25] Kavun, I. N., Lipatov, I. I., and Zapryagaev, V. I., "Flow Effects in the Reattachment Region of Supersonic Laminar Separated Flow," *Intl. J. Heat Mass Transfer*, Vol. 129, pp. 997–1009, 2019. https://doi.org/10.1016/j.ijheatmasstransfer.2018.09.125
[26] Esquieu, S., Benitez, E., Schneider, S., and Brazier, J.-P., "Flow and Stability Analysis of a Hypersonic Boundary-Layer Over an Axisymmetric Cone-Cylinder-Flare Configuration," AIAA Paper 2019-2115, 2019. https://doi.org/10.2514/6.2019-2115
[27] Cao, S., Klioutchnikov, I, and Olivier, H., "Görtler Vortices in Hypersonic Flow on Compression Ramps," *AIAA Journal*, Vol. 57, No. 9, 2019, pp. 3874–3884. https://doi.org/10.2514/1.J057975
[28] Running, C. L., Juliano, T. J., Borg, M. P., and Kimmel, R. L., "Characterization of Post-shock Thermal Striations on a Cone/Flare," *AIAA Journal*, Vol. 58, No. 4, 2007, pp. 2352–2358. https://doi.org/10.2514/1.J059095
[29] Benitez, E., Jewell, J., Schneider, S., and Esquieu, S., "Instability Measurements on an Axisymmetric Separation Bubble at Mach 6," AIAA Paper 2020-3072, 2020. https://doi.org/10.2514/6.2020-3072
[30] Benitez, E., Jewell, J., and Schneider, S., "Separation Bubble Variation Due to Small Angles of Attack for an Axisymmetric Model at Mach 6," AIAA Paper 2021-0245, 2021. https://doi.org/10.2514/6.2021-0245
[31] Cao, S., Hao, J., Klioutchnikov, I., Olivier, H., and Wen, C., "Unsteady Effects in a Hypersonic Compression Ramp Flow with Laminar Separation," *J. Fluid Mech.,* Vol. 912, A3, 2021, doi:10.1017/jfm.2020.1093
[32] Lugrin, M., Beneddine, S., Leclercq, C., Garnier, E., Bur, R., "Transition Scenario in Hypersonic Axisymmetrical Compression Ramp Flow," *J. Fluid Mech*., Vol. 907, A6, https://doi.org/10.1017/jfm.2020.833
[33] Hao, J., Cao, S., Wen, C.-Y., and Olivier, H., "Occurrence of Global Instability in Hypersonic Compression Corner Flow," *J. Fluid Mech*., Vol. 919, A4, https://doi.org/10.1017/jfm.2021.372
[34] Butler, C. S. and Laurence, S. J., "Interaction of Second-Mode Disturbances with an Incipiently Separated Compression-Corner Flow," *J. Fluid Mech.,* Vol. 913, R4, 2021, https://doi.org/10.1017/jfm.2021.91
[35] Paredes, P., Scholten, A., Choudhari, M., and Li, F., "Boundary-Layer Instabilities Over a Cone-Cylinder-Flare Model at Mach 6," AIAA Paper 2022-0600, 2022. https://doi.org/10.2514/6.2022-0600
[36] Wagner, L. N., Schneider, S. P., and Jewell, J. S., "Streamwise Vortices from Controlled Roughnesses on a Cone-Cylinder-Flare at Mach 6," AIAA Paper 2022-1671, 2022. https://doi.org/10.2514/6.2022-1671
[37] Lugrin, M., Nicolas, F., Severac, N. et al., "Transitional Shock Wave/Boundary Layer Interaction Experiments in the R2Ch Blowdown Wind Tunnel," *Exp. Fluids*, 63:46, 2022. https://doi.org/10.1007/s00348-022-03395-9

[38] Ginoux, J. J., "Streamwise Vortices in Reattaching High-Speed Flows: A Suggested Approach," *AIAA Journal*, Vol. 9, No. 4, 1971, pp. 759–760. https://doi.org/10.2514/3.6271
[39] Choudhari, M., Li, F., and Edwards, J. R., "Stability Analysis of Roughness Array Wake in a High-Speed Boundary Layer," AIAA Paper 2009-0973, 2009. https://doi.org/10.2514/6.2009-170
[40] Zaprygaev, V. I., Kavun, I. N., and Lipatov, I. I., "Supersonic Laminar Separated Flow Structure at a Ramp for a Free-stream Mach Number of 6," *Prog. Flight Phys.*, Vol. 5, 2013, pp. 349–362. https://doi.org/10.1051/eucass/201305349
[41] Litton, D., Edwards, J., and White, J., "Algorithmic Enhancements to the VULCAN Navier-Stokes Solver," AIAA Paper 2003-3979, 2003. https://doi.org/10.2514/6.2003-3979
[42] Wu, M. and Martin, M. P., "Direct Numerical Simulation of Supersonic Boundary Layer over a Compression Ramp," *AIAA Journal*, Vol. 45, No. 4, 2007, pp. 879–889. https://doi.org/10.2514/1.27021
[43] Li, F., Choudhari, M., Paredes, P., and Duan, L., "High-Frequency Instabilities of Stationary Crossflow Vortices in a Hypersonic Boundary Layer," *Phys. Rev. Fluids*, Vol. 1, 2016, 053603. https://doi.org/10.1103/PhysRevFluids.1.053603
[44] Paredes, P., Choudhari, M., Li, F., Jewell, J., and Kimmel, R., "Nonmodal Growth of Traveling Waves on Blunt Cones at Hypersonic Speeds," *AIAA Journal*, 57 (11), 2019, pp. 4738–4749.
[45] Choudhari, M., Li, F., Paredes, P., and Duan, L., "Evolution of High-Frequency Instabilities in the Presence of Azimuthally Compact Crossflow Vortex Pattern over a Yawed Cone," *Theor. Comp. Fluid Dyn.*, 2022. https://doi.org/10.1007/s00162-021-00594-8
[46] Burggraf, O. R., "Asymptotic Theory of Separation and Reattachment of a Laminar Boundary Layer on a Compression Ramp," AGARD-CP-168, Paper No. 10, 1975.
[47] Korolev, G. L., Gajjar, J. S. B., and Ruban, A. I., "Once Again on the Supersonic Flow Separation Near a Corner," *J. Fluid Mech.*, Vol. 463, pp. 173–199, 2002. https://doi.org/10.1017/S0022112002008777
[48] Gai, S. L. and Khraibut, A., "Hypersonic Compression Corner Flow with Large Separated Regions," *J. Fluid Mech.*, Vol. 477, pp. 471–494, 2019. https://doi.org/10.1017/jfm.2019.599
[49] Mack, L. M., "Boundary Layer Stability Theory," Tech. Rep. JPL Rept. 900-277, California Institute of Technology, Pasadena, CA, 1969.